

Enhancing Catalytic Conversion of Polysulfides by Hollow Bimetallic Oxide-Based Heterostructure Nanocages for Lithium-Sulfur Batteries

Yu Chen, Jiyang Li, Xiangbang Kong, Yiyong Zhang,* Yingjie Zhang, and Jinbao Zhao*

Cite This: *ACS Sustainable Chem. Eng.* 2021, 9, 10392–10402

Read Online

ACCESS |



Metrics & More



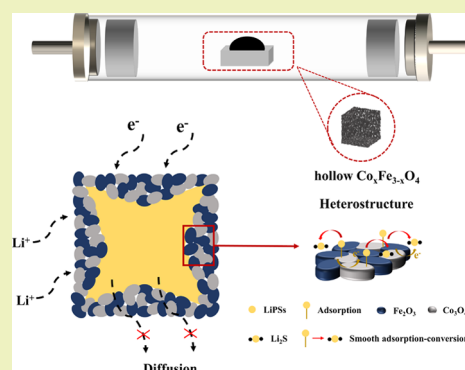
Article Recommendations



Supporting Information

ABSTRACT: Performance improvement of lithium-sulfur batteries (LSBs) is restricted by the dissolution and shuttle of lithium polysulfides (LiPSs). Prussian blue analogs (PBAs) and their derived nanomaterials are ideal sulfur-fixing materials owing to their abilities to anchor LiPSs, accelerate redox conversion, and smooth Li_2S precipitation. Herein, the hollow $\text{Co}_x\text{Fe}_{3-x}\text{O}_4$ heterostructure nanocages with highly interconnected pore architecture obtained by a PBA-assisted strategy are synthesized to overcome the abovementioned obstructions of LSBs. It is found that the bimetallic oxide-based heterostructure can not only inhibit LiPS diffusion via forming metal-sulfur bonds but also accelerate the LiPS conversion kinetics. Meanwhile, the hollow porous structure contributes to the physical confinement of LiPSs and acts as a buffer for the volume change. Thereby, the rate capability and cycling stability of hollow $\text{Co}_x\text{Fe}_{3-x}\text{O}_4@\text{S}$ composite electrodes have been improved significantly. As a result, the hollow $\text{Co}_x\text{Fe}_{3-x}\text{O}_4@\text{S}$ cell displays an excellent initial capacity of $1301.6 \text{ mAh g}^{-1}$ at a current density of 200 mA g^{-1} . Even at 1 A g^{-1} , it exhibits an outstanding initial capacity of 898.9 mAh g^{-1} with a negligible capacity loss rate, which is only 0.106% per cycle after 500 cycles. This work provides a new perspective for the construction and design of multifunctional hollow heterostructure materials for more efficient and stable LSBs.

KEYWORDS: lithium-sulfur batteries, bimetallic oxide-based heterostructure, multifunctional sulfur host, electrocatalysis, high electrochemical performance



INTRODUCTION

Recently, with the growing demand for electronic equipment with high energy and power density, the development of new rechargeable battery systems has been urgently needed. Owing to the high ideal energy density ($\sim 2500 \text{ Wh kg}^{-1}$),¹ lithium-sulfur batteries (LSBs) with high-capacity sulfur and light-weight lithium become one of the most potential nominees. Although a sulfur cathode possesses lots of advantages² (cost effectiveness, rich reserves, environmental friendliness, and superior theoretical specific capacity (1675 mAh g^{-1})), there still exist several obstacles, including the low electronic conduction of S and $\text{Li}_2\text{S}/\text{Li}_2\text{S}_2$, the large volume change, and the “shuttle effect”, which cause the loss of active materials, the damage to the electrode structure, and the fading of capacity.

To address these issues, especially to suppress the shuttling of lithium polysulfides (LiPSs), abundant methods^{3–6} have been made, which can be classified as physical confinement,⁷ chemical adsorption,⁸ and catalysis.^{9–11} Various composite materials^{12–14} have been applied as sulfur hosts, such as carbon materials,^{15–17} polymers,^{18,19} metal oxides,^{20,21} metal nitrides,²² metal sulfides,^{23,24} metal phosphides,^{25,26} etc. Among them, different carbon materials^{15,27–31} are the most

widely researched because of their superior electroconductibility and high surface areas. Nevertheless, the nonpolar carbon that served as the physical barrier for LiPSs cannot retard capacity fading after long-term cycling.³² By contrast, polar materials^{33,34} are more effective in forming strong chemical bonds with LiPSs. Furthermore, to overcome the sluggish reaction kinetics, electrocatalysis has been introduced.^{35–37} Wang *et al.* reported an Fe-doped Co_3O_4 sphere used as a sulfur host through structure design and defect fabrication.³⁸ This material has a unique structure, strong chemical adsorption ability, and abundant catalytic sites, which largely improved the performance of LSBs. Therefore, when designing a sulfur host, it is more efficient to combine physical confinement, chemical adsorption, and catalysis to suppress the shuttle effect.³⁹

Received: June 15, 2021

Revised: July 14, 2021

Published: July 23, 2021



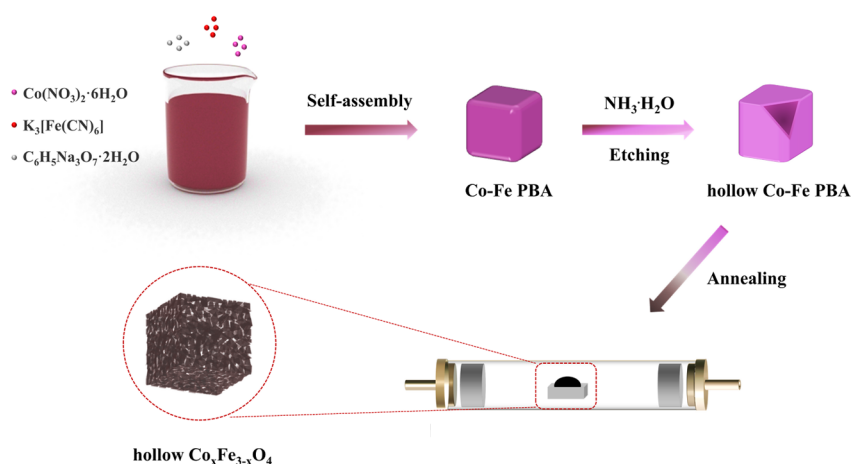


Figure 1. Synthesis diagram of the hollow $\text{Co}_x\text{Fe}_{3-x}\text{O}_4$ nanocages.

In addition, metal–organic frameworks (MOFs) and their derived materials^{40,41} have always been a hot spot in the research of LSBs, which can immobilize LiPSs and catalyze their conversion. As the representative materials of MOFs, Prussian blue (PB) and its analogs (PBAs) have drawn considerable attention owing to their tunable chemistry and the possibility to derive many other nanomaterials.⁴² In the previous research of our group,⁴³ it has been found that PB is a potential material for LSBs with improved electrochemical performance. The related nanomaterials^{25,42–48} of PB/PBAs inherit their advantages, such as the low cost, large surface area, facile synthesis, intrinsic open framework, interconnected pores, and hierarchical pore sizes, which can promote charge transfer and increase sulfur storage. Hence, a range of active nanomaterials derived from PB/PBAs used as sacrificial hosts has been studied, such as $\text{NiO-NiCo}_2\text{O}_4@\text{C}$,⁴⁹ $\text{NiO-Co}_3\text{O}_4@\text{C}$,⁵⁰ Ni-Fe-P/NC ,⁴⁷ CoP/C ,²⁵ Fe_2O_3 ,⁵¹ etc. In particular, PBA-derived bimetallic oxide-based heterostructure materials are reported to be a suitable sulfur host because bimetallic oxides have more abundant active sites and stronger interaction with polysulfides compared with monometallic oxides due to their excellent synergetic effects and hybrid orbitals,⁵² and the heterostructure can enhance the physicochemical properties of high adsorption and strong catalysis.^{39,49} Therefore, PBA-derived bimetallic oxide-based heterostructure materials are anticipated to serve as multifunctional sulfur hosts for advanced LSBs.

Herein, in order to impede the shuttle effect more effectively, the PBA-derived bimetallic oxide-based heterostructure material (hollow $\text{Co}_x\text{Fe}_{3-x}\text{O}_4$) is fabricated from the cobalt-ferrum-based Prussian blue analog (Co-Fe PBA) precursor to serve as both the sulfur host and the catalytic substrate. First, the hollow porous structure can offer more space for sulfur particles and relieve the change in volume during cycling. Second, the Co-Fe-O heterostructure nanocages have adequate chemical adsorption sites to anchor the intermediate polysulfides and facilitate polysulfide conversion. Third, the interconnected pores are conducive to the lithium ion transport and electrolyte permeation, thereby further accelerating the reaction kinetics. As a result, the hollow $\text{Co}_x\text{Fe}_{3-x}\text{O}_4@\text{S}$ electrode exhibits improved cycling stability and considerable high-rate capability.

EXPERIMENTAL SECTION

Material Synthesis. Preparation of Co-Fe PBA. In a typical synthesis, 0.02 M potassium ferricyanide solution, 0.03 M aqueous solution of cobalt nitrate, and 0.9 mmol of sodium citrate were mixed by stirring for 5 min at first and then stood for 24 h. After filtration and washing with deionized water, the precipitate was freeze-dried overnight to obtain the Co-Fe PBA precursor.

Synthesis of Hollow Co-Fe PBA. Ammonium hydroxide (5 mL) in 20 mL of deionized water was added into 20 mg of Co-Fe PBA in 10 mL of ethanol and stirred for 9 h at room temperature to form the hollow Co-Fe PBA.

Fabrication of Hollow $\text{Co}_x\text{Fe}_{3-x}\text{O}_4$. The as-prepared hollow Co-Fe PBA was annealed in O_2 at 350 °C for 6 h to obtain the hollow $\text{Co}_x\text{Fe}_{3-x}\text{O}_4$ nanocages.

Synthesis of Hollow $\text{Co}_x\text{Fe}_{3-x}\text{O}_4@\text{S}$. The hollow $\text{Co}_x\text{Fe}_{3-x}\text{O}_4$ nanocages and the sulfur particles were mixed at a certain mass ratio and then transferred to a sealed glass tube in vacuum. After that, the tube was heated at a temperature of 155 °C for 10 h to prepare the hollow $\text{Co}_x\text{Fe}_{3-x}\text{O}_4@\text{S}$ composite.

For comparison, Co_3O_4 and Fe_2O_3 were also prepared to use as the host materials via the same procedure from the cobalt-based Prussian blue analog (Co PBA) and ferrum-based Prussian blue (Fe PBA) precursors.

Material Characterization. The X-ray diffraction measurement (XRD, MiniFlex 600 Benchtop) in a range of 2θ of 5°–85° with $\text{Cu K}\alpha$ ($\lambda = 0.15418$ nm) radiation was used to characterize the crystal structure and phase of samples. The materials' morphologies, energy-dispersive spectroscopy (EDS) mapping analysis, and structures were obtained using scanning electron microscopes (SEM, TM3030, and ZEISS GeminiSEM 500) and a high-resolution transmission electron microscope (HRTEM, JEM-2100). Thermogravimetric analysis (TGA) was performed using a STA449F5 analyzer. The Brunauer-Emmett-Teller (BET) surface areas and the samples' pore diameters were obtained using an ASAP 2020 instrument. The surface elements of products were recorded by X-ray photoelectron spectroscopy (XPS, Thermo Scientific K-Alpha).

Visualized Adsorption Test. To prepare the Li_2S_6 solution, Li_2S and S (1:5 in molar ratio) were added into the solvent that contains 1,3-dioxolane (DOL) and 1,2-dimethoxyethane (DME) (1:1, v/v) with stirring at 60 °C. Subsequently, acetylene black (AB), hollow $\text{Co}_x\text{Fe}_{3-x}\text{O}_4$, Co_3O_4 , and Fe_2O_3 (20 mg) were added to 3 mL of 5 mM Li_2S_6 solution. After 24 h, the supernatant liquid was collected for the ultraviolet–visible spectrophotometry measurement (UV–vis, Lambda 1050).

Electrochemical Characterization. Li-S Cell Assembly and Measurements. The active material (hollow $\text{Co}_x\text{Fe}_{3-x}\text{O}_4@\text{S}$), AB, and a polyacrylic latex binder (LA132) were dispersed uniformly in deionized water with a mass ratio of 7:2:1, coated on the aluminum foil, and dried at 60 °C in a vacuum oven overnight to obtain the

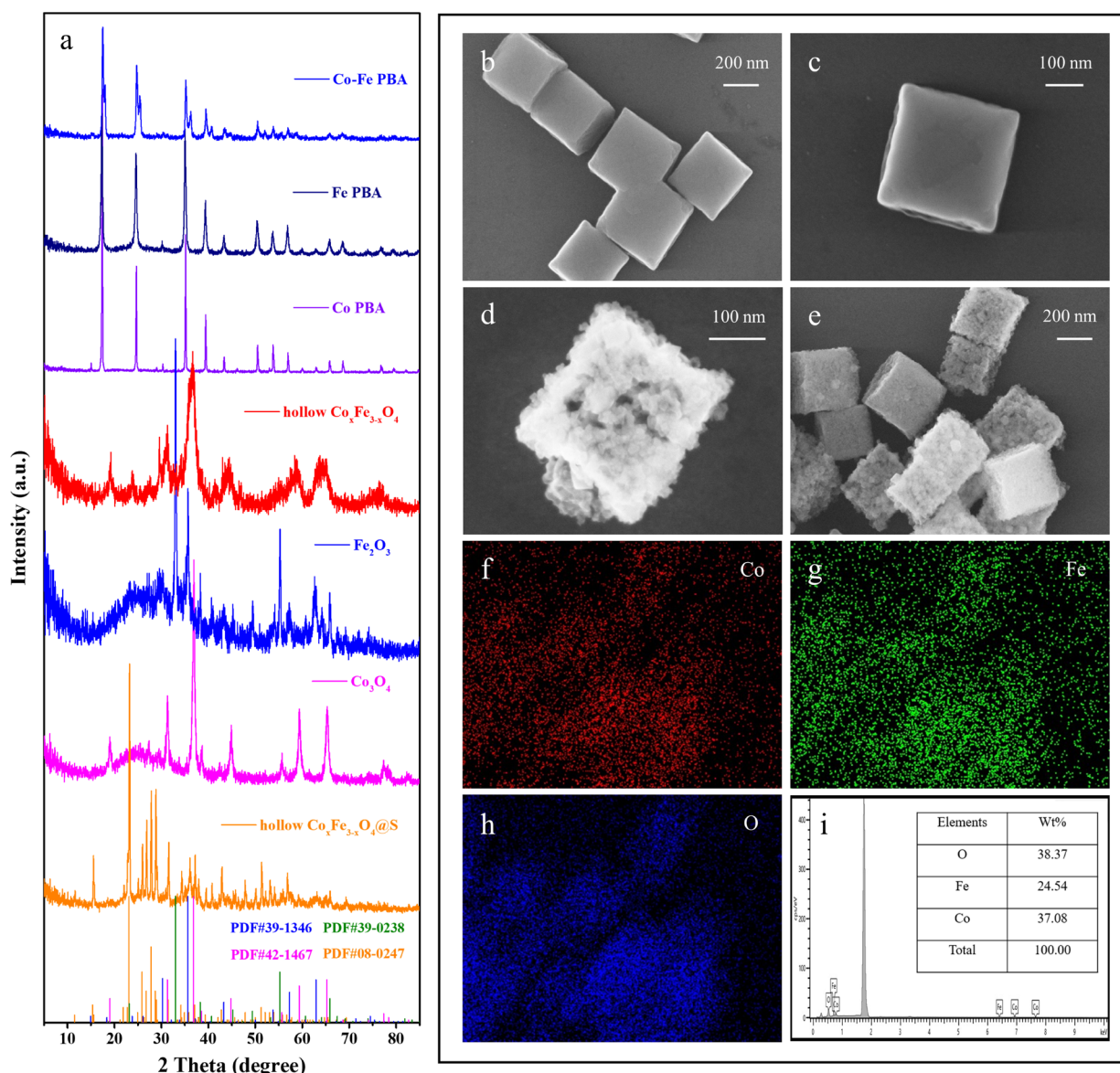


Figure 2. (a) XRD patterns of Co-Fe PBA, Co PBA, Fe PBA, hollow $\text{Co}_x\text{Fe}_{3-x}\text{O}_4$, Fe_2O_3 , Co_3O_4 , and hollow $\text{Co}_x\text{Fe}_{3-x}\text{O}_4@\text{S}$. (b–d) SEM images of Co-Fe PBA, hollow Co-Fe PBA, and hollow $\text{Co}_x\text{Fe}_{3-x}\text{O}_4$. (e–i) EDS mapping of hollow $\text{Co}_x\text{Fe}_{3-x}\text{O}_4$.

working electrodes. Then, the electrodes were punched into disks with a sulfur loading amount around 1 mg cm^{-2} . The CR2016 coin-type cells were applied for electrochemical measurements, in which the hollow $\text{Co}_x\text{Fe}_{3-x}\text{O}_4@\text{S}$ electrode, Celgard 2400 film membrane, and lithium foil were used as the working electrode, separator, and counter electrode, respectively. A traditional electrolyte ($50 \mu\text{L}$) was added to each cell. The traditional electrolyte was made by dissolving 1.0 M lithium (trifluoromethanesulfonyl) imide (LiTFSI) and a 1 wt % LiNO_3 additive into a mixed solvent of DOL and DME (1:1, v/v). The assembly process took place in an Ar-filled glove box. Cyclic voltammetry (CV) tests were recorded at diverse scan rates in a voltage region of 1.5–3.0 V using a CHI 660E electrochemical workstation and MetrohmAutolab PGSTAT-302N instrument. Galvanostatic charge and discharge (GCD) measurements were conducted on Neware battery testers in a voltage region of 1.7–2.8 V. In situ electrochemical impedance spectroscopy (EIS) was carried out using a MetrohmAutolab PGSTAT-302N from 100 kHz to 10 mHz.

Symmetric Cell Assembly and Measurements. A symmetric cell was prepared in the same way mentioned above by using the hollow $\text{Co}_x\text{Fe}_{3-x}\text{O}_4$ as an active material. For the symmetric cell, both the working and counter electrodes used the hollow $\text{Co}_x\text{Fe}_{3-x}\text{O}_4$ electrodes with $40 \mu\text{L}$ of Li_2S_6 electrolyte. The Li_2S_6 electrolyte was

made by dissolving Li_2S and S (1:5 molar ratio) into the traditional electrolyte. The symmetric cell of hollow $\text{Co}_x\text{Fe}_{3-x}\text{O}_4$ with the traditional electrolyte and the symmetrical cell of AB with the Li_2S_6 electrolyte were used for comparison. CV tests were measured at various scan rates from -1 to 1 V.

Nucleation Measurements of Lithium Sulfide. The measurements were conducted in lithium-based asymmetrical cells. The hollow $\text{Co}_x\text{Fe}_{3-x}\text{O}_4$ material (1 mg) loaded on carbon paper (CP) was applied as a working electrode with $25 \mu\text{L}$ of Li_2S_8 solution (Li_2S and S in the tetraglyme solution with a molar ratio of 1:7) as a catholyte and $25 \mu\text{L}$ of traditional electrolyte as an anolyte. For the Li_2S nucleation and growth measurement, the assembled cells remained potentiostatic at 2.05 V until the charge current was below 10^{-5} A after a galvanostatic discharge to 2.06 V.

RESULTS AND DISCUSSION

The hollow $\text{Co}_x\text{Fe}_{3-x}\text{O}_4$ nanocages are fabricated through facile and scalable methods (Figure 1). At first, the Co-Fe PBA is synthesized by the self-assembly of potassium ferricyanide, cobalt nitrate, and sodium citrate. Then, the as-prepared powder is etched by ammonia to get the hollow Co-Fe PBA

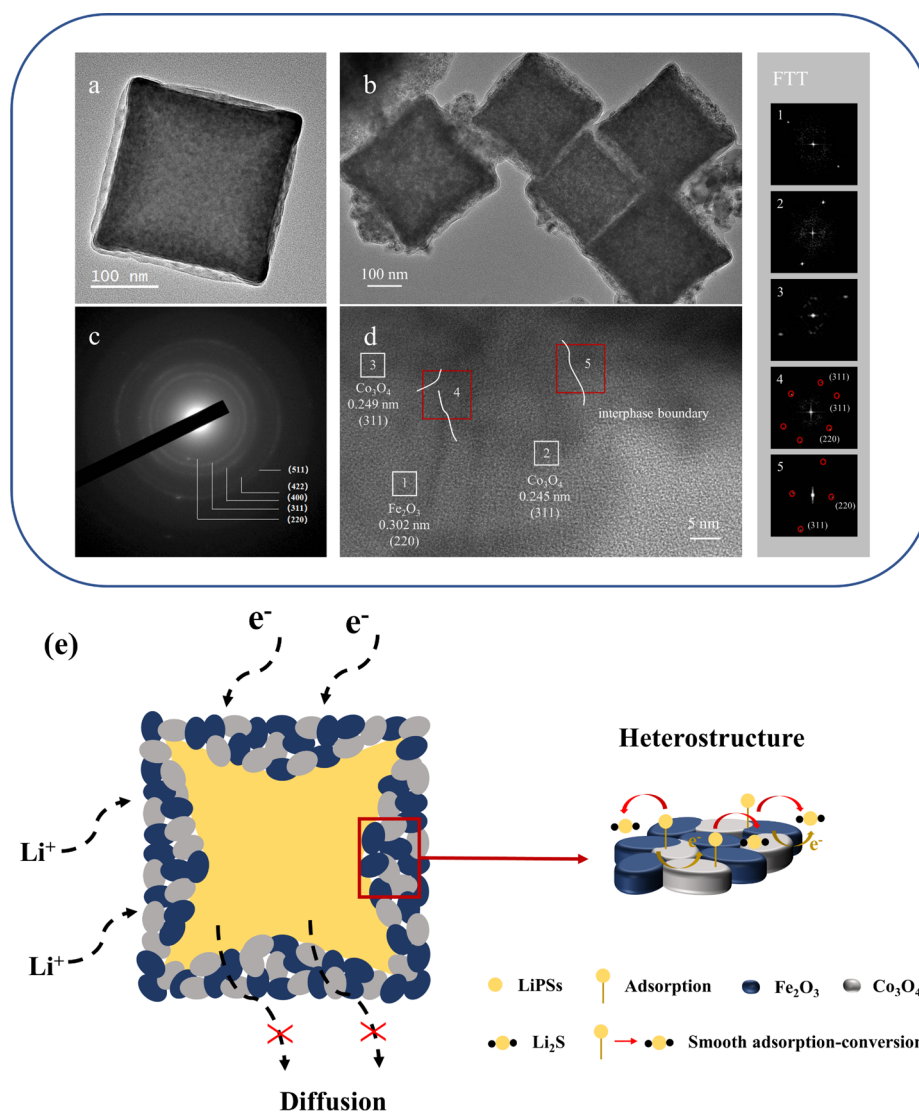


Figure 3. (a, b) TEM images of hollow Co-Fe PBA and hollow $\text{Co}_x\text{Fe}_{3-x}\text{O}_4$. (c) SAED pattern of hollow $\text{Co}_x\text{Fe}_{3-x}\text{O}_4$. (d) HRTEM image of hollow $\text{Co}_x\text{Fe}_{3-x}\text{O}_4$. (e) Scheme of the advantages of the hollow $\text{Co}_x\text{Fe}_{3-x}\text{O}_4$ @S heterostructure as LSB cathodes.

precursor. After that, the treated product is calcined in a furnace filled with oxygen to obtain the hollow $\text{Co}_x\text{Fe}_{3-x}\text{O}_4$ nanocages. Owing to the lattice defects and compressive stress during the calcination of crystal growth, the hollow $\text{Co}_x\text{Fe}_{3-x}\text{O}_4$ forms an interphase boundary called a heterostructure. In Figure 2a, the crystal structures of the as-synthesized precursors and the target products are characterized by XRD. The peaks at 18.38, 23.77, 30.24, 35.63, 43.28, 57.27, 62.93, and 74.471° are related to the (111), (210), (220), (311), (400), (511), (440), and (533) planes of Fe_2O_3 . Meanwhile, the peaks at 19.0, 31.27, 36.85, 44.8, 55.66, 59.36, 65.24, and 77.34° refer to the (111), (220), (311), (400), (422), (511), (440), and (533) planes of Co_3O_4 . The diffraction peaks of hollow $\text{Co}_x\text{Fe}_{3-x}\text{O}_4$ match well with Fe_2O_3 (PDF#39-1346) and Co_3O_4 (PDF#42-1467).

The morphologies of Co-Fe PBA, hollow Co-Fe PBA, and hollow $\text{Co}_x\text{Fe}_{3-x}\text{O}_4$ materials characterized by SEM are presented in Figure 2b–i. The Co-Fe PBA precursor exhibits a cubic shape with smooth facets and uniform particle sizes around 250–300 nm. Also, the average particle size does not change significantly during the etching process. After the calcination, it can be seen clearly that the particle maintains the

cubic morphology formed by the accumulation of abundant small nanoparticles, but the surfaces become rough and porous, which may be caused by the emission of gaseous molecules⁵³ (Figure 2d,e). This structure is beneficial for sulfur to melt into the hollow interior. EDS mapping results (Figure 2f–h) demonstrate the existence of Fe, Co, and O elements that distribute uniformly on the surface of nanocages. The surface areas and pore diameters of the hollow $\text{Co}_x\text{Fe}_{3-x}\text{O}_4$ and hollow $\text{Co}_x\text{Fe}_{3-x}\text{O}_4$ @S are obtained by the BET test. The results prove that sulfur indeed infiltrates into the channels (Figure S1).

TEM and HRTEM are performed to further investigate the structures and morphologies of the hollow Co-Fe PBA and hollow $\text{Co}_x\text{Fe}_{3-x}\text{O}_4$. Figure 3a clearly shows a four-pointed star-like hollow structure of the particles after ammonia etching (hollow Co-Fe PBA). Also, the cubic cage structure is maintained during the annealing process in oxygen (Figure 3b). The unique hollow structure could achieve high sulfur loading, prevent the outward diffusion of LiPSs, and relieve the volume change in the process of charge and discharge. In Figure 3c, the selected area electron diffraction (SAED) picture shows many dots and rings, further indicating the

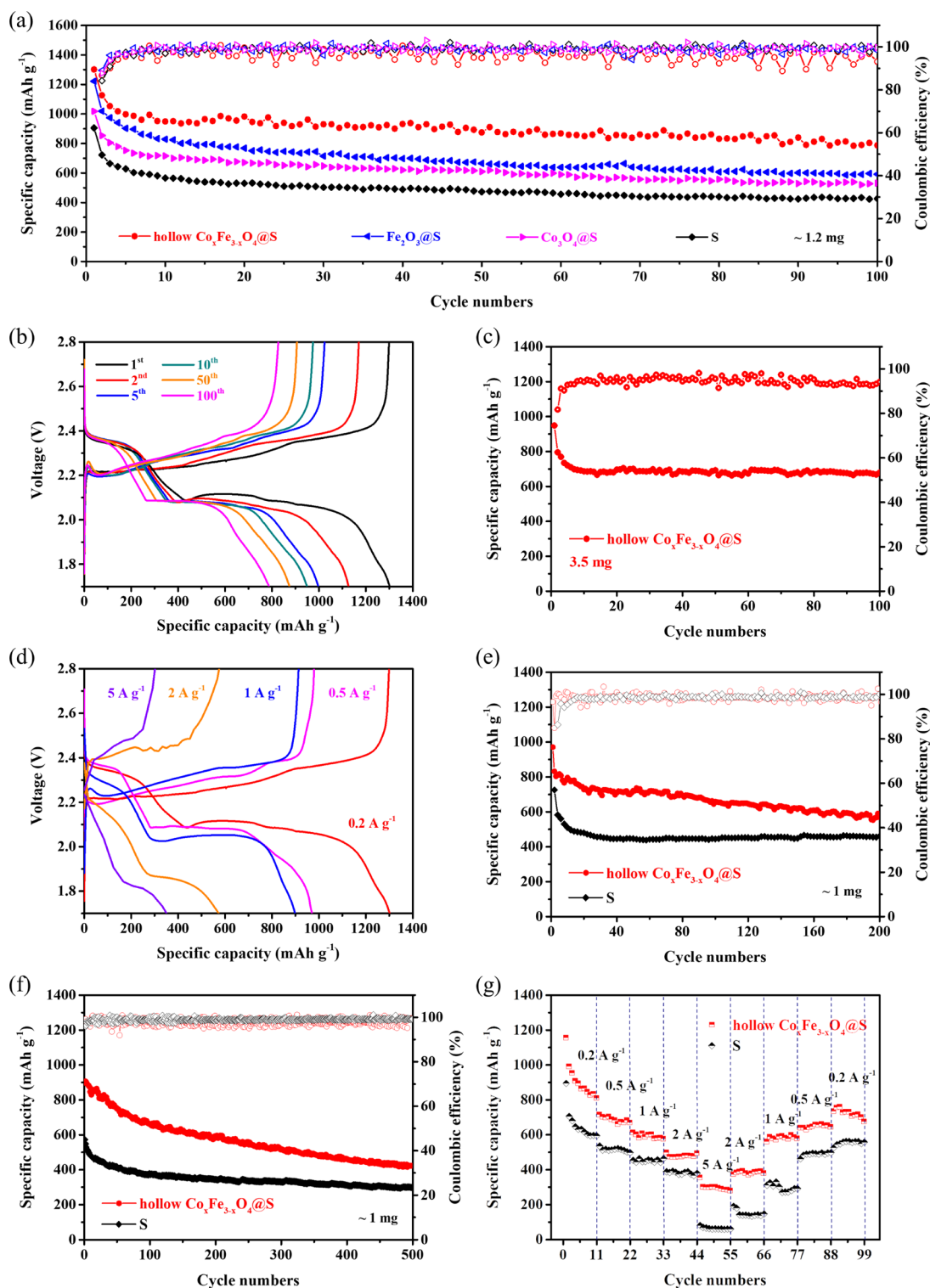


Figure 4. (a) Cycling performances of the hollow $\text{Co}_x\text{Fe}_{3-x}\text{O}_4@\text{S}$, $\text{Fe}_2\text{O}_3@\text{S}$, $\text{Co}_3\text{O}_4@\text{S}$, and sulfur cells at 0.2 A g^{-1} . (b) Discharge/charge curves at different cycles of the hollow $\text{Co}_x\text{Fe}_{3-x}\text{O}_4@\text{S}$ at 0.2 A g^{-1} . (c) Cycling performance of the hollow $\text{Co}_x\text{Fe}_{3-x}\text{O}_4@\text{S}$ cell with a high sulfur loading at 0.2 A g^{-1} . (d) Discharge/charge curves at diverse current densities of the hollow $\text{Co}_x\text{Fe}_{3-x}\text{O}_4@\text{S}$. (e) Cycling performances of the hollow $\text{Co}_x\text{Fe}_{3-x}\text{O}_4@\text{S}$ and sulfur electrodes at 0.5 A g^{-1} . (f) Long-term cycling stability of the hollow $\text{Co}_x\text{Fe}_{3-x}\text{O}_4@\text{S}$ and sulfur cells at 1 A g^{-1} . (g) Rate performances of the hollow $\text{Co}_x\text{Fe}_{3-x}\text{O}_4@\text{S}$ and sulfur cells.

presence of the crystalline (220), (311), (400), (422), and (511) phases, which is in conformity to the XRD results. The HRTEM image (Figure 3d) reveals the lattice fringe spacings of 3.02 and 2.45 Å, which are ascribed to the (220) crystal plane of Fe_2O_3 and the (311) plane of Co_3O_4 , respectively.

This observation demonstrates that the hollow $\text{Co}_x\text{Fe}_{3-x}\text{O}_4$ nanocage is a heterostructure of Fe_2O_3 and Co_3O_4 domains with intimate interfacial conjunctions, which may expedite the charge transfer and improve the LiPS conversion kinetics. The advantages of the hollow $\text{Co}_x\text{Fe}_{3-x}\text{O}_4@\text{S}$ heterostructure as

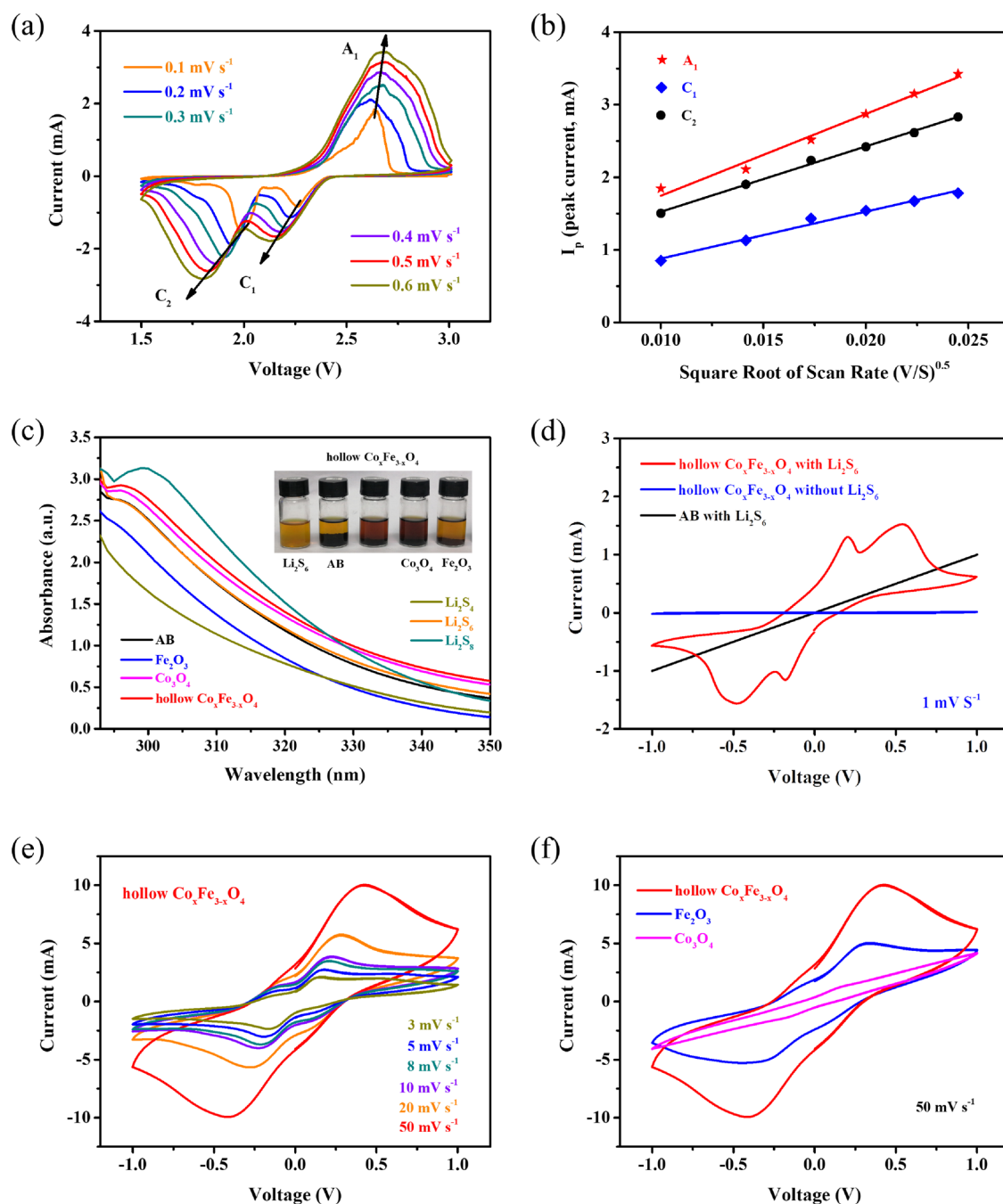


Figure 5. (a) Rate-dependent CV of the hollow $\text{Co}_x\text{Fe}_{3-x}\text{O}_4@\text{S}$. (b) Corresponding linear fitting of peak currents of the hollow $\text{Co}_x\text{Fe}_{3-x}\text{O}_4@\text{S}$. (c) Static adsorption experiments of Li_2S_6 after 12 h on AB, hollow $\text{Co}_x\text{Fe}_{3-x}\text{O}_4$, Co_3O_4 , and Fe_2O_3 with the UV–vis absorption spectrum for supernatants. (d) Polarization curves of hollow $\text{Co}_x\text{Fe}_{3-x}\text{O}_4$ symmetric cells with/without Li_2S_6 . (e) CV measurement of the hollow $\text{Co}_x\text{Fe}_{3-x}\text{O}_4$ symmetric cells at different scan rates with the 0.2 M Li_2S_6 electrolyte. (f) CV curves of the hollow $\text{Co}_x\text{Fe}_{3-x}\text{O}_4$, Fe_2O_3 , and Co_3O_4 symmetric cells at 50 mV s^{-1} .

LSB cathodes are shown in Figure 3e. The rapid lithium ion/electron transport channels, the limitation of LiPSs, and the catalytic conversion all contribute to the performance improvement.

The electrochemical performances of the hollow $\text{Co}_x\text{Fe}_{3-x}\text{O}_4@\text{S}$ applied as cathode materials for LSBs are measured in a voltage region of 1.7–2.8 V. Because the hollow $\text{Co}_x\text{Fe}_{3-x}\text{O}_4$ hosts basically do not provide capacity (Figure S2), the capacities of the cells are calculated by the sulfur mass fraction, which accounts for 73% (Figure S3). Figure 4a shows the short-term cycling performance of hollow $\text{Co}_x\text{Fe}_{3-x}\text{O}_4@\text{S}$,

$\text{Fe}_2\text{O}_3@\text{S}$, $\text{Co}_3\text{O}_4@\text{S}$, and S at 0.2 A g^{-1} . Their initial discharge capacities are 1301.6, 1221.7, 1018.1, and 905.6 mAh g^{-1} , respectively. The discharge capacities decrease to 787.6, 591.6, 531.1, and 425.8 mAh g^{-1} after 100 cycles, presenting the capacity retentions of 60.5, 48.4, 52.2, and 47%, respectively. Compared with $\text{Fe}_2\text{O}_3@\text{S}$, $\text{Co}_3\text{O}_4@\text{S}$, and S, the hollow $\text{Co}_x\text{Fe}_{3-x}\text{O}_4@\text{S}$ electrode exhibits better electrochemical performance. Figure 4b exhibits the curves of charge/discharge at different cycles. There exists two voltage plateaus in the discharge curves at approximately 2.3 and 2.1 V, which refer to the reaction reducing S_8 to LiPSs and then to $\text{Li}_2\text{S}_2/\text{Li}_2\text{S}$.

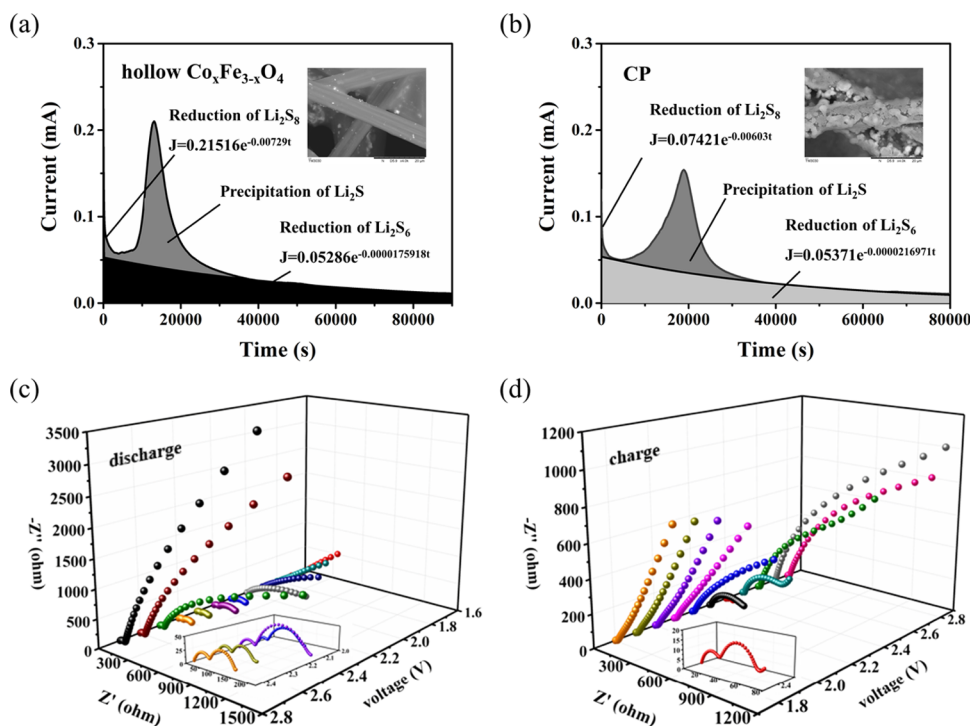


Figure 6. Current–time curves of the 0.1 M Li_2S_8 /tetraglyme solution on (a) hollow $\text{Co}_x\text{Fe}_{3-x}\text{O}_4$ and (b) bare CP substrates. In situ EIS plots of the hollow $\text{Co}_x\text{Fe}_{3-x}\text{O}_4$ @S during (c) discharge and (d) charge processes.

Moreover, even with the high sulfur loading, the hollow $\text{Co}_x\text{Fe}_{3-x}\text{O}_4$ @S material still has favorable discharge capacity (Figure 4c). The initial discharge capacities of hollow $\text{Co}_x\text{Fe}_{3-x}\text{O}_4$ @S at 0.2, 0.5, 1, 2, and 5 A g^{-1} are 1301.6, 970.4, 898.9, 573.6, and 352.9 mAh g^{-1} , respectively (Figure 4d). After 200 cycles, the hollow $\text{Co}_x\text{Fe}_{3-x}\text{O}_4$ @S electrode maintains 569.4 mAh g^{-1} at 0.5 A g^{-1} (Figure 4e). The cycle stability is further evaluated at the high current density (Figure 4f). The specific discharge capacity of the hollow $\text{Co}_x\text{Fe}_{3-x}\text{O}_4$ @S electrode remains 423 mAh g^{-1} after 500 cycles. In addition, the hollow $\text{Co}_x\text{Fe}_{3-x}\text{O}_4$ @S cell reveals good stability during the rate capability test (Figure 4g). The discharge capacity rises back to 758.4 mAh g^{-1} with the current density returning to 200 mA g^{-1} . Meanwhile, compared with most similar materials previously reported, the hollow $\text{Co}_x\text{Fe}_{3-x}\text{O}_4$ @S material exhibits comparable electrochemical performance (Table S1).

The lithium-ion diffusion coefficient (D_{Li^+}) achieved by rate-dependent CV (Figure 5a) is used for investigating the conversion kinetics of LiPSs. As shown in Figure 5b, the relationship between I_p and $\nu^{0.5}$ is displayed by anodic (A_1) and cathodic (C_1 and C_2) peak currents, which are associated with the conversion of Li_2S to S_8 , S_8 to LiPSs, and LiPSs to $\text{Li}_2\text{S}_2/\text{Li}_2\text{S}$, respectively. The fitted straight slopes of A_1 , C_1 , and C_2 are 112.59, 64.67, and 90.08, respectively. D_{Li^+} can be calculated on the basis of the Randles–Sevcik equation as follows:⁵⁴

$$I_p = 2.69 \times 10^5 n^{1.5} a D_{\text{Li}^+}^{0.5} \nu^{0.5} C_{\text{Li}} \quad (1)$$

in which I_p represents the peak current, C_{Li} refers to the lithium-ion concentration, ν corresponds to the scanning rate, D_{Li^+} is the lithium-ion diffusion coefficient, a represents the apparent surface area, and n refers to the electron transfer number. Compared with the bare sulfur cell (Figure S4), the slope of C_1 of the hollow $\text{Co}_x\text{Fe}_{3-x}\text{O}_4$ @S is larger, suggesting a

higher D_{Li^+} . The faster lithium-ion diffusion and greater reaction kinetics of the hollow $\text{Co}_x\text{Fe}_{3-x}\text{O}_4$ @S electrode can contribute to better electrochemical performance.

To assess the adsorption ability of the hollow $\text{Co}_x\text{Fe}_{3-x}\text{O}_4$, the Li_2S_6 solution is used for the adsorption test. As shown in the inset of Figure 5c, comparing the blank solution with others, the color of the supernatant after adding AB powder hardly changes, while those of Fe_2O_3 , Co_3O_4 , and hollow $\text{Co}_x\text{Fe}_{3-x}\text{O}_4$ become darker after standing for 12 h. The unexpected color change could be caused by the floating materials in the electrolyte.⁵⁵ All the supernatants are tested by UV–vis absorption spectroscopy after dilution. From the results, the order of absorption peak intensities of supernatants is as follows: hollow $\text{Co}_x\text{Fe}_{3-x}\text{O}_4 > \text{Co}_3\text{O}_4 > \text{AB} > \text{Fe}_2\text{O}_3$, which may be associated with the chemical interaction, physical precipitation, and especially chemical reaction.^{55,56}

Accelerating reaction kinetics requires not only suitable adsorption force but also strong catalysis. The catalytic capability of the hollow $\text{Co}_x\text{Fe}_{3-x}\text{O}_4$ is verified by the symmetric cells. Figure 5d displays the polarization curves of the symmetric cells. The current of hollow $\text{Co}_x\text{Fe}_{3-x}\text{O}_4$ in the absence of Li_2S_6 can almost be neglected. The current of the hollow $\text{Co}_x\text{Fe}_{3-x}\text{O}_4$ cell with the Li_2S_6 electrolyte is much higher than that of the AB cell, suggesting the boost of the electrochemical reactions of LiPSs.^{55,57} More importantly, when the scan rates increase, the CV curves preserve the original shapes with the peak currents increasing and shifting (Figure 5e). It suggests that the hollow $\text{Co}_x\text{Fe}_{3-x}\text{O}_4$ material has an excellent catalytic ability for LiPS conversion.⁵⁸ Compared with Fe_2O_3 and Co_3O_4 , the current of hollow $\text{Co}_x\text{Fe}_{3-x}\text{O}_4$ significantly increases (Figure 5f), demonstrating that the bimetallic oxide-based heterostructure accelerates the reversible conversion of LiPSs.^{59,60}

To further investigate the kinetics, the Li_2S electrodeposition on CP is characterized. In Figure 6a,b, a monotonic reduction

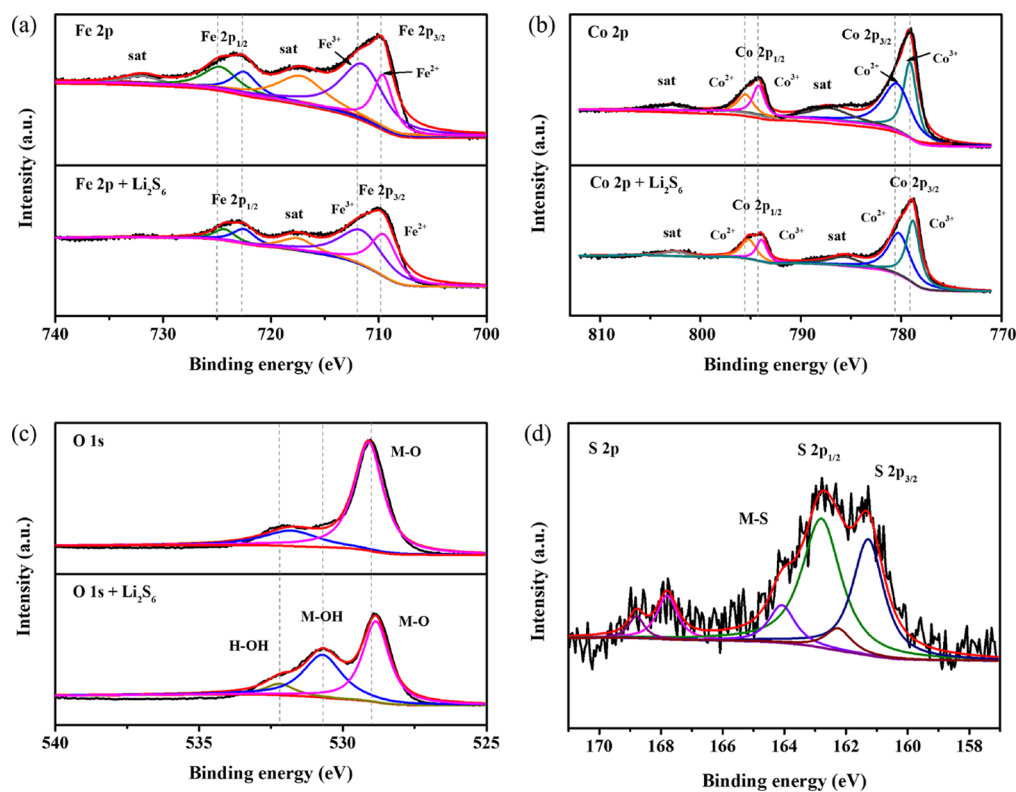


Figure 7. XPS spectra of the hollow $\text{Co}_x\text{Fe}_{3-x}\text{O}_4$ nanocages before and after adsorbing Li_2S_6 : (a) Fe 2p, (b) Co 2p, (c) O 1s, and (d) S 2p.

current during an initial “incubation” period is observed, corresponding to the reduction from $\text{Li}_2\text{S}_8/\text{Li}_2\text{S}_6$ to Li_2S_4 in solution.⁶¹ After this period, there occurs a current peak, which can be attributed to the nucleation of solid Li_2S with growth to impingement.⁶¹ The Li_2S nucleation capabilities are recorded by the current.⁶² It is clear that the time of the maximum current of hollow $\text{Co}_x\text{Fe}_{3-x}\text{O}_4$ is around 13,110 s, which is earlier than that of CP (18,890 s). The earlier and higher current peak (Figure 6a,b) indicates the enhancement of the deposition kinetics on CP with hollow $\text{Co}_x\text{Fe}_{3-x}\text{O}_4$.⁵⁷ The inset SEM images in Figure 6a,b reveal the deposition morphology of Li_2S on the carbon fiber. By comparison, it turns out that the lithium sulfide is deposited more uniformly and smoothly on the carbon fiber with the hollow $\text{Co}_x\text{Fe}_{3-x}\text{O}_4$ nanocages, proving the outstanding electrocatalytic activity of the bimetallic oxide-based heterostructure for the redox reaction of LiPSs.

The in situ EIS measurement is performed to comprehend the charge transfer at the interface of the electrode and electrolyte.⁶³ An EIS plot consists of the electrolyte resistance (an intersection at high frequency, R_o), the solid electrolyte interface resistance (a semicircle at high frequency, R_s), the charge transport impedance (a semicircle in middle frequency, R_{ct}), and the diffusion impedance (a sloping tail in low frequency).⁶⁴ During the discharge process (Figure 6c), the R_o increases from 2.4 to 2.1 V. It is suspected that the generation of LiPSs may enlarge the electrolyte viscosity, thereby impeding the transport of lithium ions.⁶³ When the formation of Li_2S starts to occur (<2.1 V), the resistance begins to decrease because of the soluble species consumption. The variations of R_s and R_{ct} are related to the formation of $\text{Li}_2\text{S}_2/\text{Li}_2\text{S}$ and the decrease of S_8 . At the initial discharge, the R_{ct} decreases because of the diminution of solid sulfur, which

remains as a more porous structure that enlarges the surface and increases the charge transport. After that, the insulating layer is formed on the electrode, leading to a smaller electroactive surface and poor conductivity, resulting in the increase of R_{ct} .⁶⁵ In addition, in Figure 6d, the evolution during the charge process is just the opposite. During the processes of charge and discharge, the uniformity of Li_2S and sulfur on the electrode surface is beneficial to reduce the impedance (Figure S5) and accelerate the reaction kinetics, which can improve the electrochemical performance.

XPS is used to analyze the valence states of the elements and the surface-adsorbed species. Figure S6 presents the peaks of the Fe 2p, Co 2p, K 2p, and O 1s of the hollow $\text{Co}_x\text{Fe}_{3-x}\text{O}_4$. The Co 2p and Fe 2p spectra consist of two shake-up satellites and two spin-orbit (Figure 7a,b). For the spectra of Fe 2p before adsorption (Figure 7a), it can be deconvoluted into Fe $2p_{1/2}$ and Fe $2p_{3/2}$. The existence of the Fe^{2+} species is confirmed by the peaks around 709.6 and 722.48 eV, while the peaks at 711.5 and 724.7 eV indicate the subsistence of Fe^{3+} in the material. Similarly, Figure 7b exhibits the spectra of Co 2p. The peaks at 779.1 and 794.2 eV can be assigned to the Co^{3+} ion in the material, whereas the peaks near 780.4 and 795.5 eV are attributed to the Co^{2+} ion.⁵³ After adsorbing Li_2S_6 , the peak positions of Co 2p and Fe 2p shift to lower binding energies, reflecting the strong interaction between Co/Fe atoms and Li_2S_6 molecules.⁶⁶ In addition, the O 1s spectra in Figure 7c indicate the existence of different oxygen species, which belongs to metal–O (529.1 eV) and surface OH^- groups (531.8 eV). After adsorption, the peaks at 530.7 and 532.2 eV could be attributed to metal–OH and H–OH formed by moisture/oxygen. Figure 7d shows the spectra of S 2p. There are four peaks at 164.08, 162.8, 162.25, and 161.28 eV, corresponding to metal–S, S $2p_{1/2}$, and S $2p_{3/2}$.^{67,68} Overall,

the bimetallic oxide-based heterogeneous structure can inhibit the LiPS diffusion by forming metal–sulfur bonds.

CONCLUSIONS

In summary, the hollow $\text{Co}_x\text{Fe}_{3-x}\text{O}_4$ heterostructure nanocages are fabricated through an energy-efficient method and employed as a sulfur host for LSBs. The hollow and porous structure enlarges the sulfur loading amount. In addition, the Fe-Co-O heterostructure anchors polysulfides, accelerates the LiPS conversion, and smooths the deposition of Li_2S . The rate-dependent CV test and in situ EIS manifest the good lithium-ion diffusion and electron transfer capabilities. Furthermore, the adsorption experiments and XPS spectra attest suitable chemical bonding of the hollow $\text{Co}_x\text{Fe}_{3-x}\text{O}_4$ with polysulfides. Equally important, the CV of symmetrical cells and the Li_2S precipitation test demonstrate the excellent catalysis of the hollow $\text{Co}_x\text{Fe}_{3-x}\text{O}_4$ heterostructure, which ameliorates the LiPS conversion kinetics. Therefore, the electrochemical performances of the hollow $\text{Co}_x\text{Fe}_{3-x}\text{O}_4@S$ material are greatly promoted. When the sulfur loading amount is about 3.5 mg cm^{-2} , the cells with the hollow $\text{Co}_x\text{Fe}_{3-x}\text{O}_4@S$ exhibit remarkable cycling stability. The capacity retention is 71.6% of the initial specific capacity (948 mAh g^{-1}). The present study is believed to give a new view on the defect engineering of bimetallic oxides as sulfur hosts and their applications in LSBs.

ASSOCIATED CONTENT

Supporting Information

The Supporting Information is available free of charge at <https://pubs.acs.org/doi/10.1021/acssuschemeng.1c04036>.

N_2 adsorption–desorption isotherms; cycling performance of the hollow $\text{Co}_x\text{Fe}_{3-x}\text{O}_4$ electrode; TGA curve of hollow $\text{Co}_x\text{Fe}_{3-x}\text{O}_4@S$; CV curves; EIS plots after 100 cycles; XPS spectra; SEM images of electrodes before and after 500 cycles; and comparison of different cathode materials (PDF)

AUTHOR INFORMATION

Corresponding Authors

Yiyong Zhang – National and Local Joint Engineering Laboratory for Lithium-ion Batteries and Materials Preparation Technology, Key Laboratory of Advanced Battery Materials of Yunnan Province, Faculty of Metallurgical and Energy Engineering, Kunming University of Science and Technology, Kunming 650093, P.R. China; Email: zhangyiyong2018@kust.edu.cn

Jinbao Zhao – State Key Laboratory of Physical Chemistry of Solid Surfaces, State-Province Joint Engineering Laboratory of Power Source Technology for New Energy Vehicle, Collaborative Innovation Center of Chemistry for Energy Materials, College of Chemistry and Chemical Engineering, Xiamen University, Xiamen 361005, P.R. China; orcid.org/0000-0002-2753-7508; Email: jbzhao@xmu.edu.cn

Authors

Yu Chen – State Key Laboratory of Physical Chemistry of Solid Surfaces, State-Province Joint Engineering Laboratory of Power Source Technology for New Energy Vehicle, Collaborative Innovation Center of Chemistry for Energy Materials, College of Chemistry and Chemical Engineering, Xiamen University, Xiamen 361005, P.R. China

Jiyang Li – State Key Laboratory of Physical Chemistry of Solid Surfaces, State-Province Joint Engineering Laboratory of Power Source Technology for New Energy Vehicle, Collaborative Innovation Center of Chemistry for Energy Materials, College of Chemistry and Chemical Engineering, Xiamen University, Xiamen 361005, P.R. China

Xiangbang Kong – State Key Laboratory of Physical Chemistry of Solid Surfaces, State-Province Joint Engineering Laboratory of Power Source Technology for New Energy Vehicle, Collaborative Innovation Center of Chemistry for Energy Materials, College of Chemistry and Chemical Engineering, Xiamen University, Xiamen 361005, P.R. China

Yingjie Zhang – National and Local Joint Engineering Laboratory for Lithium-ion Batteries and Materials Preparation Technology, Key Laboratory of Advanced Battery Materials of Yunnan Province, Faculty of Metallurgical and Energy Engineering, Kunming University of Science and Technology, Kunming 650093, P.R. China

Complete contact information is available at: <https://pubs.acs.org/10.1021/acssuschemeng.1c04036>

Author Contributions

Y.C. contributed in conceptualization, methodology, investigation, and original draft preparation of the study. J.L. aided in data curation and reviewing & editing the paper. X.K. contributed in the study's visualization. Yiyong Zhang assisted in acquiring resources and reviewing & editing the paper. Yingjie Zhang supervised and assisted in providing resources. J.Z. administrated the project and contributed in funding acquisition.

Notes

The authors declare no competing financial interest.

ACKNOWLEDGMENTS

The authors gratefully acknowledge the National Natural Science Foundation of China (21875198) and the Natural Science Foundation of Yunnan Province (202001 AU070079).

REFERENCES

- Weret, M. A.; Jeffrey Kuo, C.-F.; Zeleke, T. S.; Beyene, T. T.; Tsai, M.-C.; Huang, C.-J.; Berhe, G. B.; Su, W.-N.; Hwang, B.-J. Mechanistic understanding of the Sulfurized-Poly(acrylonitrile) cathode for lithium-sulfur batteries. *Energy Storage Mater.* **2020**, *26*, 483–493.
- Manthiram, A.; Fu, Y.; Chung, S. H.; Zu, C.; Su, Y. S. Rechargeable lithium-sulfur batteries. *Chem. Rev.* **2014**, *114*, 11751–11787.
- Deng, C.; Wang, Z.; Wang, S.; Yu, J. Inhibition of polysulfide diffusion in lithium–sulfur batteries: mechanism and improvement strategies. *J. Mater. Chem. A* **2019**, *7*, 12381–12413.
- Jana, M.; Xu, R.; Cheng, X.-B.; Yeon, J. S.; Park, J. M.; Huang, J.-Q.; Zhang, Q.; Park, H. S. Rational design of two-dimensional nanomaterials for lithium–sulfur batteries. *Energy Environ. Sci.* **2020**, *13*, 1049–1075.
- Li, Z.; Xiao, Z.; Li, P.; Meng, X.; Wang, R. Enhanced Chemisorption and Catalytic Effects toward Polysulfides by Modulating Hollow Nanoarchitectures for Long-Life Lithium–Sulfur Batteries. *Small* **2020**, *16*, 1906114.
- Wang, P.; Xi, B.; Huang, M.; Chen, W.; Feng, J.; Xiong, S. Emerging Catalysts to Promote Kinetics of Lithium–Sulfur Batteries. *Adv. Energy Mater.* **2021**, *11*, 2002893.
- Yuan, H.; Nai, J.; Fang, Y.; Lu, G.; Tao, X.; Lou, X. W. D. Double-Shelled $\text{C}@\text{MoS}_2$ Structures Preloaded with Sulfur: An

Additive Reservoir for Stable Lithium Metal Anodes. *Angew. Chem.* **2020**, *59*, 15839–15843.

(8) Peng, Y.; Zhang, Y.; Wang, Y.; Shen, X.; Wang, F.; Li, H.; Hwang, B.-J.; Zhao, J. Directly Coating a Multifunctional Interlayer on the Cathode via Electrospinning for Advanced Lithium–Sulfur Batteries. *ACS Appl. Mater. Interfaces* **2017**, *9*, 29804–29811.

(9) Wang, S.; Chen, H.; Liao, J.; Sun, Q.; Zhao, F.; Luo, J.; Lin, X.; Niu, X.; Wu, M.; Li, R.; Sun, X. Efficient Trapping and Catalytic Conversion of Polysulfides by VS₄ Nanosites for Li–S Batteries. *ACS Energy Lett.* **2019**, *4*, 755–762.

(10) Zeng, P.; Liu, C.; Zhao, X.; Yuan, C.; Chen, Y.; Lin, H.; Zhang, L. Enhanced Catalytic Conversion of Polysulfides Using Bimetallic Co₂Fe₃ for High-Performance Lithium–Sulfur Batteries. *ACS Nano* **2020**, *14*, 11558–11569.

(11) Liu, D.; Zhang, C.; Zhou, G.; Lv, W.; Ling, G.; Zhi, L.; Yang, Q. H. Catalytic Effects in Lithium–Sulfur Batteries: Promoted Sulfur Transformation and Reduced Shuttle Effect. *Adv. Sci.* **2018**, *5*, 1700270.

(12) Agostini, M.; Matic, A. Designing Highly Conductive Functional Groups Improving Guest–Host Interactions in Li/S Batteries. *Small* **2020**, *16*, 1905585.

(13) Xiong, C.; Zhu, G. Y.; Jiang, H. R.; Chen, Q.; Zhao, T. S. Achieving multiplexed functionality in a hierarchical MXene-based sulfur host for high-rate, high-loading lithium-sulfur batteries. *Energy Storage Mater.* **2020**, *33*, 147–157.

(14) Zhou, L.; Huang, T.; Yu, A. Three-Dimensional Flower-Shaped Activated Porous Carbon/Sulfur Composites as Cathode Materials for Lithium–Sulfur Batteries. *ACS Sustainable Chem. Eng.* **2014**, *2*, 2442–2447.

(15) Peng, Y.; Zhang, Y.; Huang, J.; Wang, Y.; Li, H.; Hwang, B. J.; Zhao, J. Nitrogen and oxygen dual-doped hollow carbon nanospheres derived from catechol/polyamine as sulfur hosts for advanced lithium sulfur batteries. *Carbon* **2017**, *124*, 23–33.

(16) Chulliyote, R.; Hareendrakrishnakumar, H.; Joseph, M. G. Hierarchical Porous Carbon Material with Multifunctionalities Derived from Honeycomb as a Sulfur Host and Laminated on the Cathode for High-Performance Lithium–Sulfur Batteries. *ACS Sustainable Chem. Eng.* **2019**, *7*, 19344–19355.

(17) Zhang, J.; Yang, C.-P.; Yin, Y.-X.; Wan, L.-J.; Guo, Y.-G. Sulfur Encapsulated in Graphitic Carbon Nanocages for High-Rate and Long-Cycle Lithium–Sulfur Batteries. *Adv. Mater.* **2016**, *28*, 9539–9544.

(18) Cui, Y.; Fu, Y. Enhanced Cyclability of Li/Polysulfide Batteries by a Polymer-Modified Carbon Paper Current Collector. *ACS Appl. Mater. Interfaces* **2015**, *7*, 20369–20376.

(19) Xu, Y.; Zheng, D.; Ji, W.; Abu-Zahra, N.; Qu, D. A molecular dynamics study of the binding effectiveness between undoped conjugated polymer binders and tetra-sulfides in lithium–sulfur batteries. *Composites, Part B* **2021**, *206*, 108531.

(20) Lin, J.-X.; Qu, X.-M.; Wu, X.-H.; Peng, J.; Zhou, S.-Y.; Li, J.-T.; Zhou, Y.; Mo, Y.-X.; Ding, M.-J.; Huang, L.; Sun, S.-G. NiCo₂O₄/CNF Separator Modifiers for Trapping and Catalyzing Polysulfides for High-Performance Lithium–Sulfur Batteries with High Sulfur Loadings and Lean Electrolytes. *ACS Sustainable Chem. Eng.* **2021**, *9*, 1804–1813.

(21) Zhou, Y.; Shu, H.; Zhou, Y.; Sun, T.; Han, M.; Chen, Y.; Chen, M.; Chen, Z.; Yang, X.; Wang, X. Flower-like Bi₄Ti₃O₁₂/Carbon nanotubes as reservoir and promoter of polysulfide for lithium sulfur battery. *J. Power Sources* **2020**, *453*, 227896.

(22) Tu, J.; Li, H.; Lan, T.; Zeng, S.-Z.; Zou, J.; Zhang, Q.; Zeng, X. Facile synthesis of TiN nanocrystals/graphene hybrid to chemically suppress the shuttle effect for lithium-sulfur batteries. *J. Alloys Compd.* **2020**, *822*, 153751.

(23) Yao, S.; Zhang, C.; Guo, R.; Majeed, A.; He, Y.; Wang, Y.; Shen, X.; Li, T.; Qin, S. CoS₂-Decorated Cobalt/Nitrogen Co-Doped Carbon Nanofiber Networks as Dual Functional Electrocatalysts for Enhancing Electrochemical Redox Kinetics in Lithium–Sulfur Batteries. *ACS Sustainable Chem. Eng.* **2020**, *8*, 13600–13609.

(24) Zeng, Z.; Li, W.; Chen, X.; Zhang, N.; Qi, H.; Liu, X. Nanosized FeS₂ Particles Caged in the Hollow Carbon Shell as a Robust Polysulfide Adsorbent and Redox Mediator. *ACS Sustainable Chem. Eng.* **2020**, *8*, 3261–3272.

(25) Lin, J.; Zhang, K.; Zhu, Z.; Zhang, R.; Li, N.; Zhao, C. CoP/C Nanocubes-Modified Separator Suppressing Polysulfide Dissolution for High-Rate and Stable Lithium–Sulfur Batteries. *ACS Appl. Mater. Interfaces* **2020**, *12*, 2497–2504.

(26) Zhang, F.; Li, Z.; Cao, T.; Qin, K.; Xu, Q.; Liu, H.; Xia, Y. Multishelled Ni₂P Microspheres as Multifunctional Sulfur Host 3D-Printed Cathode Materials Ensuring High Areal Capacity of Lithium–Sulfur Batteries. *ACS Sustainable Chem. Eng.* **2021**, *9*, 6097–6106.

(27) Zhang, Y.; Li, K.; Huang, J.; Wang, Y.; Peng, Y.; Li, H.; Wang, J.; Zhao, J. Preparation of monodispersed sulfur nanoparticles-partly reduced graphene oxide-polydopamine composite for superior performance lithium-sulfur battery. *Carbon* **2017**, *114*, 8–14.

(28) He, G.; Evers, S.; Liang, X.; Cuisinier, M.; Garsuch, A.; Nazar, L. F. Tailoring Porosity in Carbon Nanospheres for Lithium–Sulfur Battery Cathodes. *ACS Nano* **2013**, *7*, 10920–10930.

(29) Zhang, B.; Xiao, M.; Wang, S.; Han, D.; Song, S.; Chen, G.; Meng, Y. Novel Hierarchically Porous Carbon Materials Obtained from Natural Biopolymer as Host Matrixes for Lithium–Sulfur Battery Applications. *ACS Appl. Mater. Interfaces* **2014**, *6*, 13174–13182.

(30) Gao, T.; Yu, Z.; Huang, Z.-H.; Yang, Y. Nitrogen/Oxygen Dual-Doped Carbon Nanofibers as an Electrocatalytic Interlayer for a High Sulfur Content Lithium–Sulfur Battery. *ACS Applied Energy Materials* **2019**, *2*, 777–787.

(31) Yin, L.; Wang, J.; Lin, F.; Yang, J.; Nuli, Y. Polyacrylonitrile/graphene composite as a precursor to a sulfur-based cathode material for high-rate rechargeable Li–S batteries. *Energy Environ. Sci.* **2012**, *5*, 6966–6972.

(32) Lin, L.; Pei, F.; Peng, J.; Fu, A.; Cui, J.; Fang, X.; Zheng, N. Fiber network composed of interconnected yolk-shell carbon nanospheres for high-performance lithium-sulfur batteries. *Nano Energy* **2018**, *54*, 50–58.

(33) Gao, H.; Ning, S.; Zou, J.; Men, S.; Zhou, Y.; Wang, X.; Kang, X. The electrocatalytic activity of BaTiO₃ nanoparticles towards polysulfides enables high-performance lithium–sulfur batteries. *J. Energy Chem.* **2020**, *48*, 208–216.

(34) Huang, Y.; Lv, D.; Zhang, Z.; Ding, Y.; Lai, F.; Wu, Q.; Wang, H.; Li, Q.; Cai, Y.; Ma, Z. Co-Fe bimetallic sulfide with robust chemical adsorption and catalytic activity for polysulfides in lithium-sulfur batteries. *Chem. Eng. J.* **2020**, *387*, 124122.

(35) Shi, Z.; Sun, Z.; Cai, J.; Fan, Z.; Jin, J.; Wang, M.; Sun, J. Boosting Dual-Directional Polysulfide Electrocatalysis via Bimetallic Alloying for Printable Li–S Batteries. *Adv. Funct. Mater.* **2021**, *31*, 2006798.

(36) Liu, Y.; Wei, Z.; Zhong, B.; Wang, H.; Xia, L.; Zhang, T.; Duan, X.; Jia, D.; Zhou, Y.; Huang, X. O-, N-Coordinated single Mn atoms accelerating polysulfides transformation in lithium-sulfur batteries. *Energy Storage Mater.* **2021**, *35*, 12–18.

(37) Li, Z.; Zhou, C.; Hua, J.; Hong, X.; Sun, C.; Li, H.-W.; Xu, X.; Mai, L. Engineering Oxygen Vacancies in a Polysulfide-Blocking Layer with Enhanced Catalytic Ability. *Adv. Mater.* **2020**, *32*, 1907444.

(38) Wang, W.; Zhao, Y.; Zhang, Y.; Wang, J.; Cui, G.; Li, M.; Bakenov, Z.; Wang, X. Defect-Rich Multishelled Fe-Doped Co₃O₄ Hollow Microspheres with Multiple Spatial Confinements to Facilitate Catalytic Conversion of Polysulfides for High-Performance Li–S Batteries. *ACS Appl. Mater. Interfaces* **2020**, *12*, 12763–12773.

(39) Huang, S.; Wang, Z.; Von Lim, Y.; Wang, Y.; Li, Y.; Zhang, D.; Yang, H. Y. Recent Advances in Heterostructure Engineering for Lithium–Sulfur Batteries. *Adv. Energy Mater.* **2021**, *11*, 2003689.

(40) Zhang, Z.; Huang, Y.; Liu, X.; Chen, C.; Xu, Z.; Liu, P. Zeolitic imidazolate frameworks derived ZnS/Co₃S₄ composite nanoparticles doping on polyhedral carbon framework for efficient lithium/sodium storage anode materials. *Carbon* **2020**, *157*, 244–254.

(41) Chen, S.; Luo, J.; Li, N.; Han, X.; Wang, J.; Deng, Q.; Zeng, Z.; Deng, S. Multifunctional LDH/Co₉S₈ heterostructure nanocages as

high-performance lithium–sulfur battery cathodes with ultralong lifespan. *Energy Storage Mater.* **2020**, *30*, 187–195.

(42) Chen, J.; Wei, L.; Mahmood, A.; Pei, Z.; Zhou, Z.; Chen, X.; Chen, Y. Prussian blue, its analogues and their derived materials for electrochemical energy storage and conversion. *Energy Storage Mater.* **2020**, *25*, 585–612.

(43) Peng, Y.; Li, B.; Wang, Y.; He, X.; Huang, J.; Zhao, J. Prussian Blue: A Potential Material to Improve the Electrochemical Performance of Lithium–Sulfur Batteries. *ACS Appl. Mater. Interfaces* **2017**, *9*, 4397–4403.

(44) Song, X.; Song, S.; Wang, D.; Zhang, H. Prussian Blue Analogs and Their Derived Nanomaterials for Electrochemical Energy Storage and Electrocatalysis. *Small Methods* **2021**, *5*, 2001000.

(45) Hurlbutt, K.; Wheeler, S.; Capone, L.; Pasta, M. Prussian Blue Analogs as Battery Materials. *Joule* **2018**, *2*, 1950–1960.

(46) Nai, J.; Lou, X. W. D. Hollow Structures Based on Prussian Blue and Its Analogs for Electrochemical Energy Storage and Conversion. *Adv. Mater.* **2019**, *31*, 1706825.

(47) Chen, X.; Zeng, S.; Muheyati, H.; Zhai, Y.; Li, C.; Ding, X.; Wang, L.; Wang, D.; Xu, L.; He, Y.; Qian, Y. Double-Shelled Ni–Fe–P/N-Doped Carbon Nanobox Derived from a Prussian Blue Analogue as an Electrode Material for K-Ion Batteries and Li–S Batteries. *ACS Energy Lett.* **2019**, *4*, 1496–1504.

(48) Hu, Q.; Wang, Z.; Huang, X.; Qin, Y.; Yang, H.; Ren, X.; Zhang, Q.; Liu, J.; He, C. A unique space confined strategy to construct defective metal oxides within porous nanofibers for electrocatalysis. *Energy Environ. Sci.* **2020**, *13*, 5097–5103.

(49) Hu, L.; Dai, C.; Liu, H.; Li, Y.; Shen, B.; Chen, Y.; Bao, S.-J.; Xu, M. Double-Shelled NiO–NiCo₂O₄ Heterostructure@Carbon Hollow Nanocages as an Efficient Sulfur Host for Advanced Lithium–Sulfur Batteries. *Adv. Energy Mater.* **2018**, *8*, 1800709.

(50) Huang, G.; Yin, D.; Zhang, F.; Li, Q.; Wang, L. Yolk@Shell or Concave Cubic NiO–Co₃O₄@C Nanocomposites Derived from Metal–Organic Frameworks for Advanced Lithium–Ion Battery Anodes. *Inorg. Chem.* **2017**, *56*, 9794–9801.

(51) Zhao, C.; Shen, C.; Xin, F.; Sun, Z.; Han, W. Prussian blue-derived Fe₂O₃/sulfur composite cathode for lithium–sulfur batteries. *Mater. Lett.* **2014**, *137*, 52–55.

(52) Wang, W.; Li, J.; Jin, Q.; Liu, Y.; Zhang, Y.; Zhao, Y.; Wang, X.; Nurpeissova, A.; Bakenov, Z. Rational Construction of Sulfur-Deficient NiCo₂S_{4–x} Hollow Microspheres as an Effective Polysulfide Immobilizer toward High-Performance Lithium/Sulfur Batteries. *ACS Appl. Energy Mater.* **2021**, *4*, 1687–1695.

(53) Kang, L.; Ren, H.; Xing, Z.; Zhao, Y.; Ju, Z. Hierarchical porous Co_xFe_{3–x}O₄ nanocubes obtained by calcining Prussian blue analogues as anodes for lithium-ion batteries. *New J. Chem.* **2020**, *44*, 12546–12555.

(54) Huang, X.; Wang, Z.; Knibbe, R.; Luo, B.; Ahad, S. A.; Sun, D.; Wang, L. Cyclic Voltammetry in Lithium–Sulfur Batteries—Challenges and Opportunities. *Energy Technol.* **2019**, *7*, 1801001.

(55) Feng, S.; Zhong, H.; Song, J.; Zhu, C.; Dong, P.; Shi, Q.; Liu, D.; Li, J.; Chang, Y.-C.; Beckman, S. P.; Song, M.-k.; Du, D.; Lin, Y. Catalytic Activity of Co–X (X = S, P, O) and Its Dependency on Nanostructure/Chemical Composition in Lithium–Sulfur Batteries. *ACS Appl. Energy Mater.* **2018**, *1*, 7014–7021.

(56) Jeon, J.; Jeong, J. W.; Jung, Y. S. Titanium(III) Sulfide Nanoparticles Coated with Multicomponent Oxide (Ti–S–O) as a Conductive Polysulfide Scavenger for Lithium–Sulfur Batteries. *Electron. Mater. Lett.* **2019**, *15*, 613–622.

(57) Qiu, Y.; Fan, L.; Wang, M.; Yin, X.; Wu, X.; Sun, X.; Tian, D.; Guan, B.; Tang, D.; Zhang, N. Precise Synthesis of Fe–N₂ Sites with High Activity and Stability for Long-Life Lithium–Sulfur Batteries. *ACS Nano* **2020**, *14*, 16105–16113.

(58) Li, S.; Xu, P.; Aslam, M. K.; Chen, C.; Rashid, A.; Wang, G.; Zhang, L.; Mao, B. Propelling polysulfide conversion for high-loading lithium–sulfur batteries through highly sulfiphilic NiCo₂S₄ nanotubes. *Energy Storage Mater.* **2020**, *27*, 51–60.

(59) Yuan, Z.; Peng, H.-J.; Hou, T.-Z.; Huang, J.-Q.; Chen, C.-M.; Wang, D.-W.; Cheng, X.-B.; Wei, F.; Zhang, Q. Powering Lithium–

Sulfur Battery Performance by Propelling Polysulfide Redox at Sulfiphilic Hosts. *Nano Lett.* **2016**, *16*, 519–527.

(60) Kim, S. J.; Kim, K.; Park, J.; Sung, Y. E. Role and Potential of Metal Sulfide Catalysts in Lithium–Sulfur Battery Applications. *ChemCatChem* **2019**, *11*, 2373–2387.

(61) Fan, F. Y.; Carter, W. C.; Chiang, Y. M. Mechanism and Kinetics of Li₂S Precipitation in Lithium–Sulfur Batteries. *Adv. Mater.* **2015**, *27*, 5203–5209.

(62) Ma, F.; Wan, Y.; Wang, X.; Wang, X.; Liang, J.; Miao, Z.; Wang, T.; Ma, C.; Lu, G.; Han, J.; Huang, Y.; Li, Q. Bifunctional Atomically Dispersed Mo–N₂/C Nanosheets Boost Lithium Sulfide Deposition/Decomposition for Stable Lithium–Sulfur Batteries. *ACS Nano* **2020**, *14*, 10115–10126.

(63) Zhao, Z.; Yi, Z.; Li, H.; Pathak, R.; Yang, Z.; Wang, X.; Qiao, Q. Synergetic effect of spatially separated dual co-catalyst for accelerating multiple conversion reaction in advanced lithium sulfur batteries. *Nano Energy* **2021**, *81*, 105621.

(64) Waluś, S.; Barchasz, C.; Bouchet, R.; Alloin, F. Electrochemical impedance spectroscopy study of lithium–sulfur batteries: Useful technique to reveal the Li/S electrochemical mechanism. *Electrochim. Acta* **2020**, *359*, 136944.

(65) Qiu, X.; Hua, Q.; Zheng, L.; Dai, Z. Study of the discharge/charge process of lithium–sulfur batteries by electrochemical impedance spectroscopy. *RSC Adv.* **2020**, *10*, 5283–5293.

(66) Chen, Y.; Zhang, W.; Zhou, D.; Tian, H.; Su, D.; Wang, C.; Stockdale, D.; Kang, F.; Li, B.; Wang, G. Co–Fe Mixed Metal Phosphide Nanocubes with Highly Interconnected-Pore Architecture as an Efficient Polysulfide Mediator for Lithium–Sulfur Batteries. *ACS Nano* **2019**, *13*, 4731–4741.

(67) Liu, T.; Yang, F.; Cheng, G.; Luo, W. Reduced Graphene Oxide-Wrapped Co_{9–x}Fe_xS₈/Co,Fe–N–C Composite as Bifunctional Electrocatalyst for Oxygen Reduction and Evolution. *Small* **2018**, *14*, 1703748.

(68) Chen, G.; Li, Y.; Zhong, W.; Zheng, F.; Hu, J.; Ji, X.; Liu, W.; Yang, C.; Lin, Z.; Liu, M. MOFs-derived porous Mo₂C–C nano-octahedrons enable high-performance lithium–sulfur batteries. *Energy Storage Mater.* **2020**, *25*, 547–554.